

Concurrent Unsteady Surface Pressure Field and Schlieren Measurements of the Common Front End Hypersonic Geometry in Transonic Conditions

Connor Marshall[1], Nick Heath[2], Dan Handford[2], Jason Smith[2], Peter Manovski[1], Terence Avadiar[1], Malcolm Jones[1] & Andrew Neely[2]

1 Defence Science and Technology Group (DSTG), Port Melbourne VIC 3207, Australia
2 School of Engineering and Technology, The University of New South Wales, Canberra ACT 2612, Australia

Abstract

An experimental test campaign was completed in the DSTG Transonic Wind Tunnel (TWT) demonstrating a new concurrent background oriented schlieren (BOS) and unsteady pressure sensitive paint (PSP) capability, greatly advancing previous published work [1][2][3]. The single-camera concurrent measurement technique overcomes the challenges of limited optical access plaguing many industrial wind tunnel facilities. PSP measurements are acquired with high-speed BOS in alternating frames on the same camera to enable the time series field measurements to be correlated and compared. The test campaign was conducted on the Common Front End (CFE) hypersonic geometry [4] developed in collaboration between UNSW and Lockheed Martin Australia (LMA) supported by Defence Trailblazer. The on-board pressure and temperature data acquisition system designed for flight was tested and enabled PSP validation. Inclusion of a six degree-of-freedom (6DOF) force balance yielded a complete data package providing valuable insight into the transonic performance of hypersonic vehicles and a framework for future testing.

Keywords: non-intrusive measurement, flight performance, pressure sensitive paint, background oriented schlieren, experimental measurement.

1. Introduction

Hypersonic vehicles must transit the transonic speed range, whether during boost or final phase, particularly when designed for reusability. The transonic performance of designs optimised for high-speed flight is not well understood and may be complex and highly non-linear. Unsteady shock structures, or buffet, and pressure fluctuations may stress the vehicle locally or induce unexpected control feedback; thereby necessitating an assessment of vehicle aerodynamic performance in off-design stages of its flight envelope.

Literature on the transonic performance of hypersonic vehicles is focused on launch system performance and on the multi-regime, computational optimisation of glide vehicles and waveriders. In the rocket literature, steady schlieren and pressure sensitive paint (PSP) assessment of multiple rocket forebody shapes has previously enabled the correlation of shocks with pressure drops and expansion with pressure rise but no dynamics were captured [5][6]. A high-speed PSP and schlieren assessment of the IC3X geometry at Mach 7.2 resulted in a similar comparison for hypersonic conditions but, since the schlieren was not captured concurrently, the pressure dynamics were not correlated with shock dynamics [7]. The high-fidelity experimental investigations of the NASA space launch system (SLS) and launch vehicle payload fairings have used PSP to assess the impact of strakes and payload fairings on transonic buffet [8][9][10], enabling high spatio-temporal resolution of surface pressure fields. This is notably the only unsteady PSP results on a rocket geometry in transonic conditions but no schlieren was captured. The computational investigations for SLS provide

a “gold-standard” flow visualisation for these problems with a numerical schlieren and surface pressure field [11][12]. Aside from the transonic focused studies, multiple “wide-speed-range” optimisation studies on hypersonic glide vehicles have demonstrated an interest in the transonic regime though they generally use lower fidelity models and lack detailed experimental validation [13][14][15][16][17][18].

This test campaign progresses this body of work through testing of the Common Front End (CFE) hypersonic flight vehicle jointly developed by Lockheed-Martin Australia (LMA) and the University of New South Wales (UNSW) as a high-speed testbed [4]. The primary objective of this investigation was to experimentally capture high spatial and temporal resolution concurrent PSP and BOS data in transonic conditions on a single camera. A concurrent measurement refers to a quasi-simultaneous (alternating-frame) acquisition such that the results are essentially synchronised. Capturing these results in an industrial test facility is challenging and required major development of the existing DSTG optical measurement capability [1][2][3]. The developed capability provides a wealth of valuable data for validation of CFD simulations and understanding of the driving flow phenomena.

2. Experimental Design and Optical Measurement Capability Development

2.1 Facility Description

The DSTG Transonic Wind Tunnel (TWT) is an industrial continuous flow facility driven by a primary two-stage axial flow compressor with an auxiliary compressor running a plenum evacuation system (PES). The facility can reach Mach numbers from 0.3 to 1.2 using a converging nozzle with variable back pressure controlled using the PES and Mach 1.4 can be reached using a converging-diverging nozzle. Total pressure set points within the operating limits of 30 to 200 kPa are maintained to within 0.25 kPa by the PES system and dual of vacuum pumps. The total temperature is nominally held constant at 35 °C using 6 cooling towers supplying chilled water to a primary heat exchanger in the settling chamber and a secondary heat exchanger immediately after the auxiliary compressor. The 0.8 m by 0.8 m test section has slotted top and bottom walls to enable flow through for the PES system with interchangeable slotted or solid sidewalls.

Solid sidewalls restrict optical access to a 420 mm diameter schlieren viewport while slotted walls have only a 300 mm by 70 mm rectangular window. The schlieren viewport is made from BK7, NH2/A quality, optical glass transmitting 90% of wavelengths from 350 nm to 2000 nm. Limited wiring pass-throughs into the pressure vessel restricts camera equipment and all equipment within the pressure vessel must be pressure rated. A compact and robust optical measurement system is required to overcome these constraints. The concurrent PSP-BOS system reduces the size and number of cameras without requiring setup changes while generating high quality results.

During the optical measurement portion of the test campaign, the CFE test article traversed an angle-of-attack (AOA) sweep from 0° to 10°, with azimuthal roll angles 0°, 22.5°, 45°, and 90°. Mach numbers ranging from 0.6 to 1.15 were tested at a flow stagnation condition of 60 kPa and 35°C. The conditions are summarised in Table 1 but only select data, for the purpose of evaluating the BOS and PSP system, is presented in this report. Additional testing was completed at other angles and tunnel conditions for the acquisition of aerodynamic loads and pressure tap data but did not include optical measurement.

Table 1 – Optical measurement test conditions.

Variable	Conditions
Mach	0.60, 0.70, 0.80, 0.90, 0.95, 1.00, 1.05, 1.10, 1.15
Pitch angles	0, 5, 10
Roll angles	0, 22.5

2.2 Model and On-board Instrumentation

The wind tunnel article is the full-scale CFE flight test vehicle as constructed for Flight Experiment 1 (FE1) [19] with a length (*L*) of 730 mm and a diameter (*D*) of 220 mm. The complete transonic experimental setup is shown in Figure 1 with the camera field-of-views overlaid. Note that all images within this report are horizontally flipped to match flow from left to right conventions for readability. The model is divided into three sections; the forebody, tier 1, and the transition. The three sections of the model are additively manufactured from titanium using electron beam manufacture. The CFE is mounted onto a six degree-of-freedom strain gauge balance to collect model total loads with balance moment centre positioned near the model reference centre (MRC). The balance is connected via a sting to the main support model-positioning system enabling pitch angles from – 15° to 15° and roll angles from – 180° to 180° pivoting about the MRC. Cabling must be fed through the sting and support structure to exit the test section and then out of the pressure vessel and through to the main data acquisition systems.

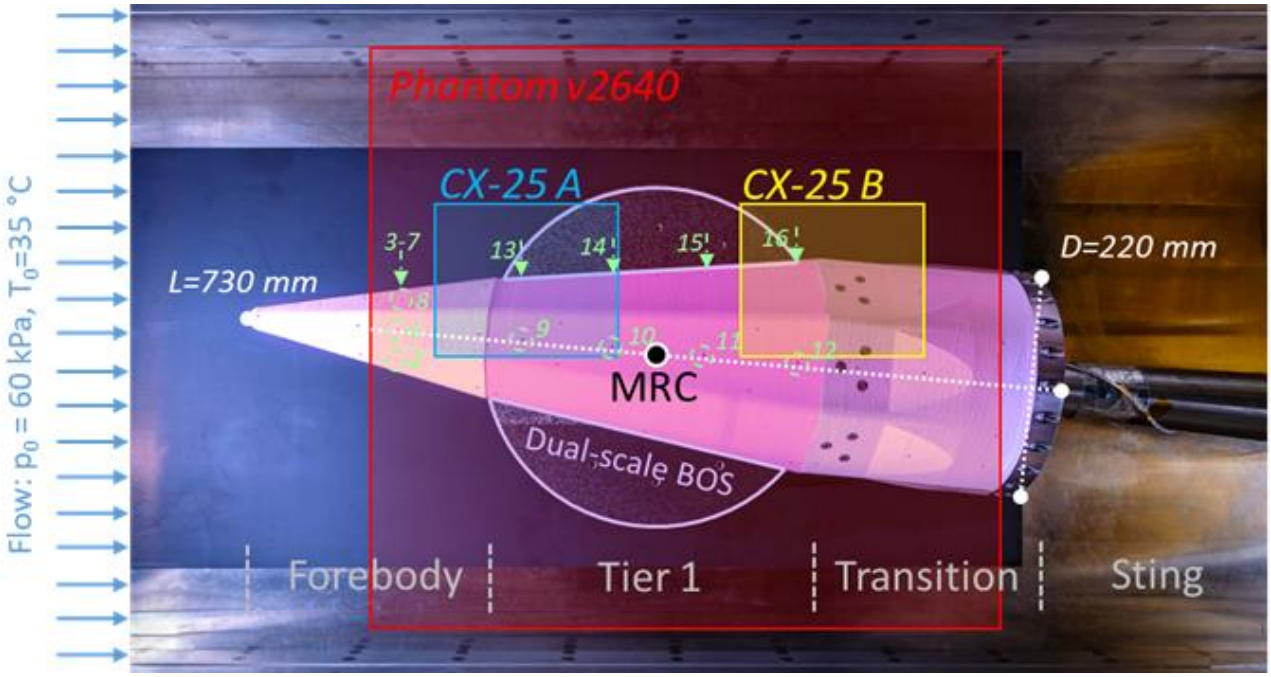


Figure 1 – Experimental setup for the CFE (pitched at 10° AOA) in the TWT with camera views overlaid. CX-25 A and CX-25 B are the upstream and downstream high-resolution cameras respectively. The CFE is separated into 3 sections visually separated by false colour tint on the PSP. Pressure taps are circled and numbered in mint green with arrows notating hidden locations. Thermocouples are only located on the tier 1 facet facing toward the camera. The dual-scale BOS region is outlined in mauve showing the restricted BOS region for the Phantom v2640.

The flight avionics hardware for the FE1 vehicle [20] was repackaged to accommodate the sting and balance adapter and reconfigured to use pressure sensors matched to the tunnel conditions and sample at a rate of 4 kHz. An array of 17 NXP MPX2100AP 0 – 100 kPa absolute analogue pressure sensors were mounted on PCB interfaces connected to the Hyperflight Systems IS-FB17 instrumentation serialiser. Tubing of 1/8” diameter connected the pressure taps to the sensors limiting the frequency response closer to 1 kHz. Eight type K thermocouples embedded in 2 mm deep thermowells in the 4 mm thick walls of the tier 1 facets were wired directly to the Hyperflight Systems IS-TB17 thermocouple serializer and sampled at 1 kHz. The Hyperflight devices streamed the pressure and temperature data through RS422 to the on-board Raspberry Pi 5, which consolidated the data and relayed it to the control room over Ethernet and was used to configure the devices through RS485.

Each of the 8 facets of the vehicle forebody have a single pressure tapping at a fixed axial location, with an additional row of four pressure taps situated on the vehicle mid-body on both opposing faces, as shown in Figure 1. The pressure transducers are barbed to accept a 1/8” flexible tube to transmit the pressure from the model surface to the transducer situated on a PCB board in the model’s interior. The vehicle rear booster connection is terminated by a truncated flat base on which additional pressure taps were placed to allow base flow measurements and corrections.

2.3 Optical Instrumentation

The optical system combined 3 cameras with 10 lights mounted from an optical table beneath the test section using a rigid support structure as depicted in Figure 2. A critical design requirement of the PSP and BOS system was compactness, as it was required to fit within the constrained 420 mm diameter optical access of the TWT schlieren window. Furthermore, routine removal of the side wall was necessary to allow access to the model for configuration changes and setup modifications. To accommodate these constraints, the system was cantilever-mounted from an optical table beneath the test section and supported on linear rails equipped with a dual-pivot folding mechanism.

A Phantom v2640 camera (2048 × 1952 pixel with pixel pitch 13.5 µm) with a Zeiss Milvus 25 mm f/1.4 lens operated at an aperture of $f_{\#}$ = 8 is placed in the centre to be used for wide field-of-view unsteady measurements. An Edmund Optics Dark Red 600-720 nm bandpass filter was fitted and removes the shorter wavelength ultraviolet (UV) PSP excitation light from the longer wavelength emission spectra whilst still allowing ample broadband BOS lighting to be collected. Situated either side are two high-resolution LaVision CX-25 Imagers (5312 × 4600 pixels with pixel pitch 2.7 µm) fitted with a 24 mm focal length lens operated at an aperture of $f_{\#}$ = 8. The cameras are focussed on the regions of interest at the interface locations between each CFE section. The addition of the second Imager expands the BOS system of Humphreys et al. (2022) enabling an increased field of view while maintaining spatial resolution. Dark red 635-690 nm bandpass filters are installed on the Imager cameras to absorb UV reflections from the PSP lights.

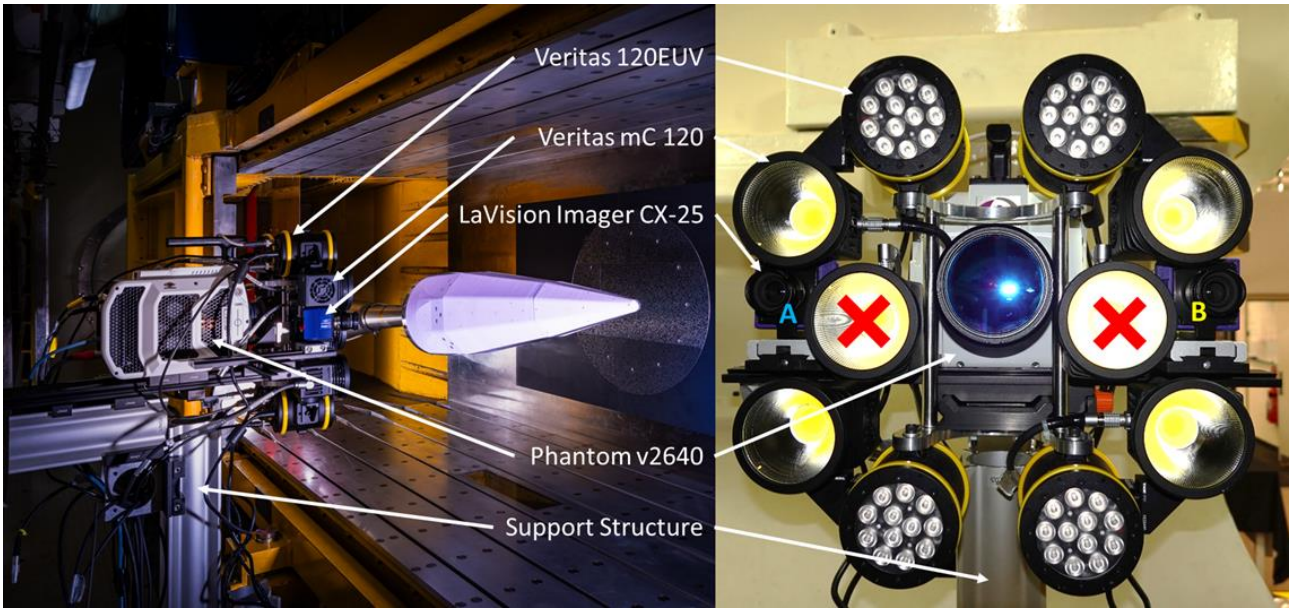


Figure 2 – In the centre of the optical setup a Phantom v2640 camera captures high-speed, wide field-of-view data while two LaVision CX-25 Imagers capture high-resolution imagery in primary regions of interest. Four UV LEDs are included for PSP measurements with six white LEDs for BOS measurements. The two central LEDs marked with a red cross were not used due to excessive reflections. The test section sidewall in the left image was removed to provide model context.

A LaVision PTU-X precision timing unit provided synchronisation. The Phantom and Imager acquisition was configured and operated separately. The LED lighting was fit around the cameras as close to the window as possible to reduce reflections. Two Veritas Constellation 120EUV (28°, 385 nm, 28 W pulsed optical output) above the Phantom and 2 below provide UV light for PSP. Six Veritas miniConstellation (mC) 120 (28°, 5000 K, 200 W pulsed optical output) positioned around the LaVision imagers provide the white light for BOS. Reflections prevented the central two BOS lights from being used bringing the total UV illumination to 112 W and the total white illumination to 800 W. The system was controlled using DaVis 11.2 on a dedicated host PC. To collect concurrent unsteady density and pressure fields, the double frame configuration was used. This setting is typically used for particle image velocimetry to acquire two images in rapid succession. The ability to command separate lasers or lights for each frame is crucial for the concurrent capability in this experiment. The first trigger was sent to the white LEDs for BOS and the second was sent to the UV lights for PSP. The cameras acquired two images such that BOS was captured on odd frames and PSP on even frames. For the Phantom v2640 high-speed imaging each light is pulsing at 3.0 kHz while the camera acquires two images per cycle essentially operating at double the frequency, 6.0 kHz. The timing diagram shown in Figure 3 summarises the DaVis control as configured for the Phantom camera, Camera 3.

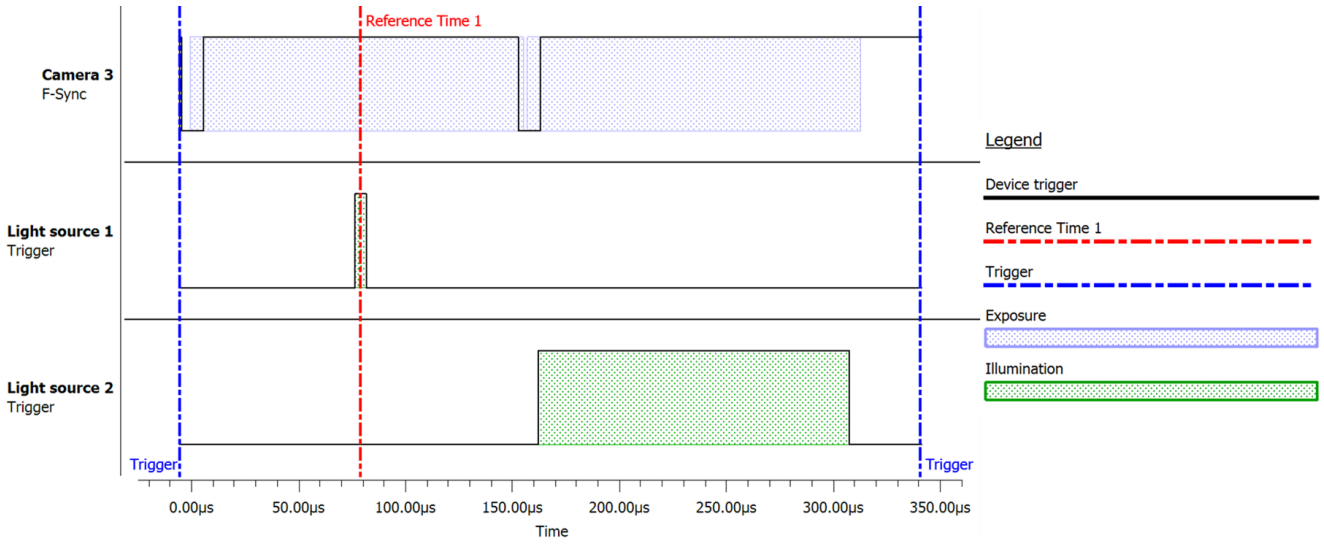


Figure 3 – Timing diagram for the triggering and capture of the Phantom v2640 frames (camera 3) aligned with the Veritas miniConstellation LEDs (light source 1) for BOS on odd frames and Veritas Constellation 120EUV 385 nm LEDs (light source 2) for PSP on the even frames.

Since the camera exposure per frame is fixed, 150 µs for the Phantom at 3.0 kHz, the image intensity must be controlled by the LED illumination time. For similar intensity levels, the brighter white LEDs, light source 1, are pulsed for much shorter duration than the UV LEDs, light source 2. For the Phantom the selected timing was 5 µs white light and 140 µs for UV light. These illumination times are displayed in green in the timing diagram and are centred on the camera exposure duration. The device trigger signals in black are relayed to the devices through BNC connections throughout the facility with each set of lights connected in series. For the Imagers acquiring double frames at 10 Hz, the frame exposure time was 2500 µs and the illumination timing was 250 µs white light and 2400 µs for UV light. The reference time, marked red, is recorded as the image pair absolute time. For each model configuration, a batch of 95 images was recorded at 10 Hz using the high-resolution cameras and a batch of 3000 images was recorded at 3.0 kHz for the high-speed camera.

2.4 Dual-scale Background Oriented Schlieren

BOS measurements were conducted using a dual-scale BOS configuration able to meet the resolution requirements of the Phantom and Imager systems. The minimum separation between the camera plane and the background pattern was approximately 0.85 m. For the Imager cameras this results in an image resolution of approximately 16 pixels/mm at the background plane, with imaged dot diameters of 2–4 pixels, suitable for robust cross-correlation. The Phantom camera with 25 mm lens achieved approximately 2 pixels/mm at the background plane.

The background pattern was designed to maximise spatial resolution while satisfying established PIV cross-correlation criteria. It was fabricated by laser etching a matte black aluminium sheet (Rosco Cinefoil BlackWrap, 0.05 mm thickness) to expose the underlying reflective surface, producing small-diameter, high-contrast dots. The etched pattern was affixed to the test section wall using clear double-sided adhesive to ensure planarity and minimise optical artefacts. The procedures used to generate, characterise and validate the etched BOS backgrounds, including assessment of dot size and contrast, are described in detail in Humphreys et al. [1] and are not repeated here.

To accommodate the differing spatial resolution requirements of the high-speed and high-resolution systems, a multi-scale BOS background was developed. For the high-speed Phantom camera, the pattern incorporated large dots with imaged diameters of approximately 2–3 pixels, ensuring robust cross-correlation despite reduced magnification. Embedded within each of these large dots were smaller unetched regions, forming fine-scale features suitable for the high-resolution cameras. Outside these regions, the background consisted exclusively of small dots, also imaged at approximately 2–3 pixels by the high-resolution cameras. As a consequence of this multi-scale design, the high-resolution cameras imaged a composite background consisting of both primary dot features and smaller embedded features within the larger dots. This raised the possibility of bias in the cross-correlation due to the presence of large-scale structures optimised for the lower-resolution high-speed system. Initial assessments indicate that these effects are minimal, with shock structures showing no significant deviation between multi-scale and equivalent single-scale backgrounds. Further quantitative evaluation is performed by Manovski et al [21].

Image acquisition and processing were performed using DaVis 11.2. Post-processing corrections caused by tunnel vibration, thereby isolating local pixel displacements associated with density gradients in the flow. Final vector fields were computed using interrogation windows of 16 × 16 pixels with 50 % overlap, yielding an effective spatial grid resolution of approximately 0.5 mm for the high-resolution cameras and 4.0 mm for the high-speed camera.

2.5 PSP Calibration

The test campaign used Innovative Scientific Solutions inc. Fast pressure sensitive paint comprised of a porous base coat to accelerate the paint response time and a lumiphore coat. The paint response is influenced by the quality of the base coat application but is expected to achieve 20 kHz response frequencies [22]. The paint is sprayed onto the three facets facing the camera using high-volume-low-pressure spray guns in a spray booth in the days prior to the test campaign.

Calibration of the PSP was necessary to quantify the relationship of PSP luminescence to air pressure to obtain global pressure data during wind-on experiments. This was achieved via exposing the PSP coated wind tunnel test article to uniform static pressures and fitting a second-order polynomial to each pixel to yield the coefficients of the characteristic Stern-Volmer equation [23]. The calibration was performed in a pixel-by-pixel manner [24] to ensure non-ideal effects of spatial non-uniformity in the PSP response were automatically compensated for which would not be possible with an *a priori* PSP calibration.

The TWT pressure control system permits an in-situ calibration of the PSP to be performed at various set pressure levels to allow accurate quantification of the paint response at expected transonic test conditions. The calibration was completed immediately after every test run to minimise the effects of paint degradation and temperature non-uniformity. From wind-on conditions, the tunnel was vacuumed down to a total pressure of 40 kPa then the main fan turned off to reach isobaric wind-off conditions. Image data was then collected at each model position executed during wind-on runs (i.e.,

0° and 10° AOA) to account for the varying camera-model view factors and the displacement of the model with respect to the fixed illumination field. Tunnel vents were then opened to increment the pressure by 10 kPa for the calibration procedure to repeat until atmospheric pressure was reached. To ensure no discrepancy between calibration and wind-on states, BOS lights were also used as per the pulsed timing sequence detailed in §2.3. Simultaneously with the PSP, the on-board pressure transducers were calibrated to later permit direct comparison of the PSP signal in the vicinity of a pressure tapping to be compared. Thermocouple measurements from the calibrations and wind-on measurements were used to quantify temperature differences for which the fast porous PSP is known to be sensitive to [25][26]. Early calibration tests found the lighting and paint to be stable for the nominal test point duration and did not require a temporal correction. It is understood that because the UV lights were pulsed with a duty cycle of less than 50 % they, and the model, did not suffer from the same heating which continuous illumination would. The lowest PSP calibration pressure was restricted to 40 kPa due to TWT operating limits.

3. Data Processing

PSP results are processed in two stages; firstly the calibration images are processed to acquire second-order polynomial fits for every pixel to convert intensity ratios to pressure, and then secondly the wind-on images are processed. The wind-on intensity, I, versus reference image intensity, I_{ref}, ratio normalises the intensity counts for each pixel, which differ due to lumiphore density, model orientation, and non-uniform illumination fields. A reference pressure, P_{ref}, of 60 kPa was originally used as it matched the total pressure during the experiment. Post-processing found that P_{ref} of 40 kPa improved the results as it was closer to the static pressure ranges on the model. A total pressure of 60 kPa was selected for the wind-on tests to increase the paint fluorescence intensity for better signal-to-noise ratio. The unintended result was that many of the measured pressures fell in the extrapolated region of the calibration curve.

The calibration procedure temporally averages the image stack captured at each pressure set point, P, before registering it against the selected 40 kPa reference image. The reference image versus the calibration images ratio produces a matrix of intensity ratios required to compute, via least-squares regression, a second-order Stern-Volmer (SV) equation fit of the form:

$$\frac{I_{ref}}{I} = A + B\frac{P}{P_{ref}} + C\left(\frac{P}{P_{ref}}\right)^2, \tag{1}$$

where the coefficients A, B and C vary spatially over the image as per the aforementioned pixel-by-pixel calibration. An average SV calibration curve is shown in Figure 4 with errors bars indicating the variability across the image which pixel-by-pixel calibration seeks to address. Model orientation, paint application, and illumination generate uncertainty in the averaged fit shown. Pixel-by-pixel calibration further reduces the uncertainty.

Before applying the Stern-Volmer calibration to wind on data, pre-processing was required. The first step of the full processing procedure, visualised in Figure 5, was to mask the imported data to reduce processing cost. Model and camera vibrations experienced during wind-on testing required image registration to realign each frame. Wind-on model deflections also generated misalignment with the calibration results so all wind-on images were registered against the reference image using MATLAB's *imregcorr* function on one-fourth down-sampled images for speed. Then the images were checked for anomalies such as lighting flickers due a noisy trigger line. Drops in the mean brightness across the frame were successfully detected to reject the anomalous images. Once the data was checked, a ratio of each image against the averaged, 40 kPa, wind-off, calibration reference image was created. Using a reference image close to the static pressure conditions provided lower noise in the calibration when the image intensity was small. The ratio images, and the calibration image, were spatially filtered to reduce noise using a Gaussian filter. Finally, the Stern-Volmer equation is rearranged and multiplied through by the reference pressure to yield quantitative global pressure datasets.

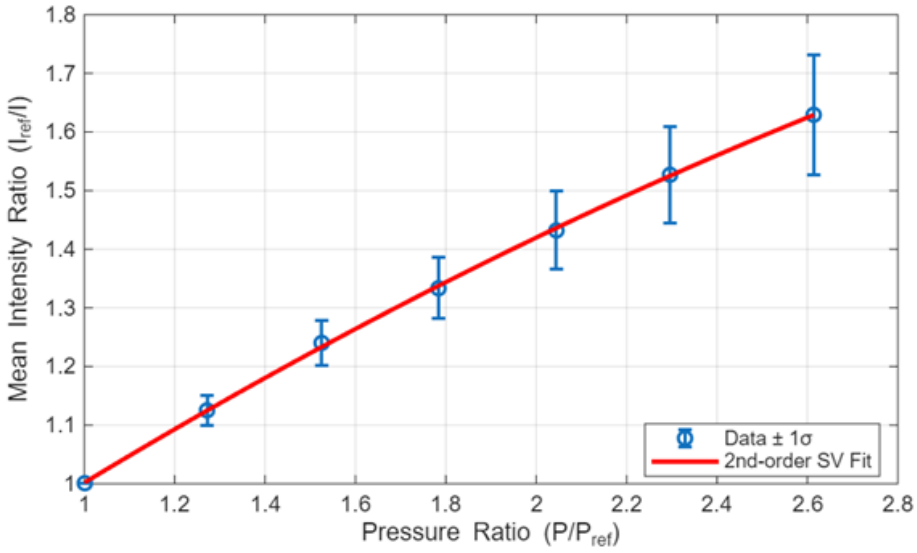


Figure 4 – The SV 2nd-order calibration is computed with a reference pressure of 40 kPa with error bars of 1 standard deviation, σ.

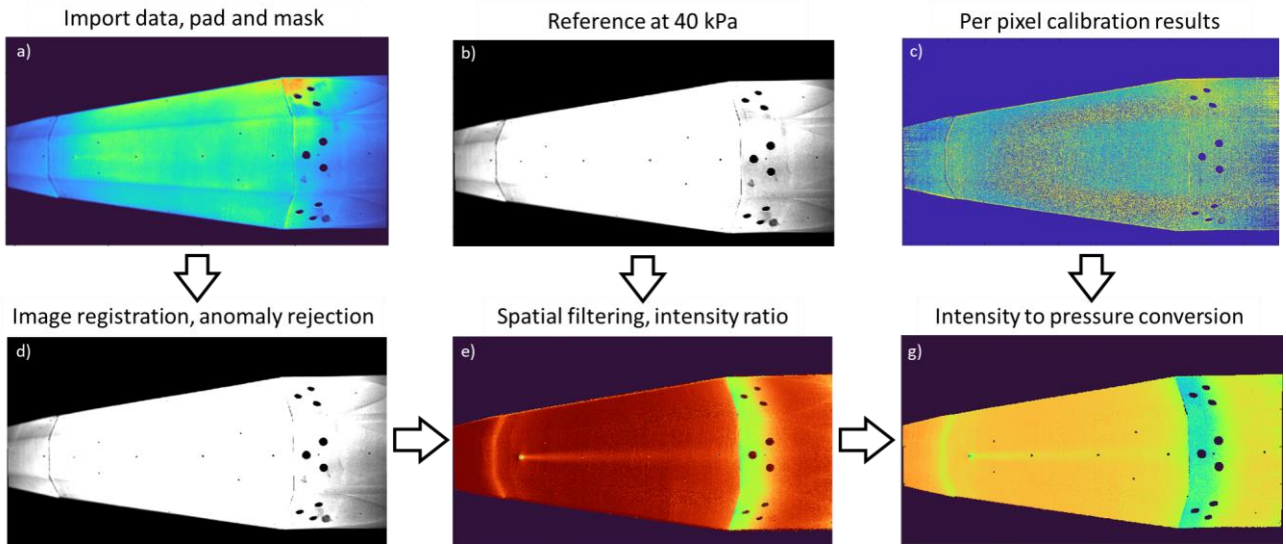


Figure 5 – Flow chart of the wind-on PSP processing procedure highlighting the pre-processing completed to correct for vibrations, smooth spatial noise, and reduce computational expense.

4. Results

4.1 Concurrent High-Resolution PSP and BOS Measurements

Unfortunately, BOS data could not be acquired by the lower resolution, high-speed camera because the wide field of view of the Phantom camera system was unable to resolve the displacements generated by the density gradients for the imaged flow field in this configuration. While the multiscale BOS pattern was effective at providing a suitable background pixel density, the effective pixel size was too large such that the displacements due to the density gradient were less than the resolvable 0.05 pixel accuracy for the cross-correlation algorithm. The very strong density gradients are required to cause a sufficient shift in the dot pattern. Additionally, the angular incidence near the edges of the frame is very high so the planar reflections of the BOS LEDs from the sidewall dot pattern are very

low intensity. The resulting image contains very high noise and low signal near the edges of the frame. This can be alleviated through positioning of the lights farther from the camera to improve the planar reflection but that is often constrained due to the limited optical access. Another option is to use retroreflective material for the BOS pattern but the high-resolution printing required for the small dot pattern has not been achievable so far. Therefore, BOS data was only available for the high-resolution (Imager) cameras with the field of view restricted due to the large model size. As such, the transition areas from forebody to tier 1 and tier 1 to transition became the focus.

BOS requires the camera to be focused on the dot pattern on the sidewall whereas the camera should be focused on the model for PSP. For a freestream test with a large model the two focal planes are far apart from one another requiring a relatively closed camera aperture to enable sufficient depth of field. To image the PSP while the focal plane was on the tunnel side wall the aperture had to be closed to $f_{\#} = 8$, greatly reducing the image intensity to single digit percentages of the camera dynamic range. The PSP results are therefore very noisy when acquired simultaneously in this fashion.

The concurrent PSP and BOS results from the upstream (CX-25 A) high-resolution Imager camera, focussed on the forebody-tier 1 interface, are presented in Figure 6. The greyscale contour map shows the horizontal displacement, which is proportional to the line-of-sight density gradient in the horizontal direction. The mean displacement across the image was subtracted as a first order vibration and bulk flow density correction. The coloured contour map displays the absolute pressure PSP results. The results are the average of 95 frames captured for Mach numbers of 0.95 and 1.15 and the exposure time of 2500 µs mean motion is not frozen.

At Mach 0.95 a low-pressure ring on the CFE is visible behind the lip at the forebody-tier 1 interface in the PSP alongside small density gradients in the vicinity. The same ring is visible in the Mach 1.15 case although the density gradients are much stronger, and a lambda shock is present at the separated low-pressure region. Comparison between the Mach 0.95 and 1.15 pressure levels shows much lower pressures for higher Mach numbers. Since the total pressure is maintained at 60 kPa the static pressure is lower for higher Mach numbers where the dynamic pressure is greater.

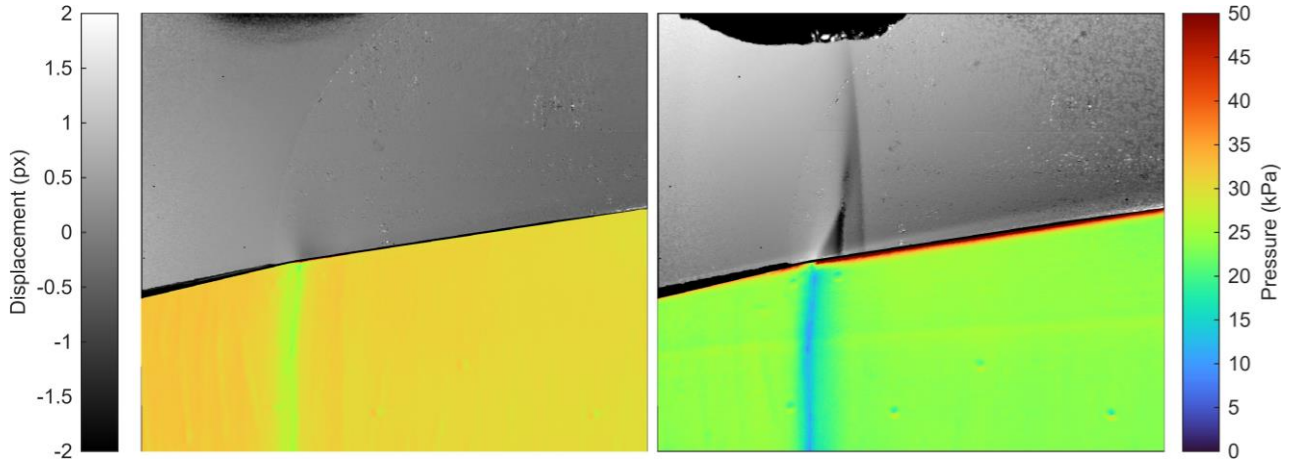


Figure 6 – Concurrent averaged BOS (grey) and PSP (colour) results from the upstream high-resolution camera (CX-25 A) at Mach 0.95 (left) and Mach 1.15 (right) at a roll angle of 0°.

The concurrent PSP and BOS results from the downstream (CX-25 B) Imager camera focussed on the tier 1-transition interface are presented in Figure 7. In both the Mach 0.95 and 1.15 cases the expansion fan at the transition results in a sharp pressure gradient on the surface leading to a low-pressure region. In the Mach 0.95 case an attached normal shock structure leads to a noticeable pressure rise whereas the oblique shock structure in the Mach 1.15 results in an extended low-pressure region and lower pressures on the transition piece compared to the tier 1 section.

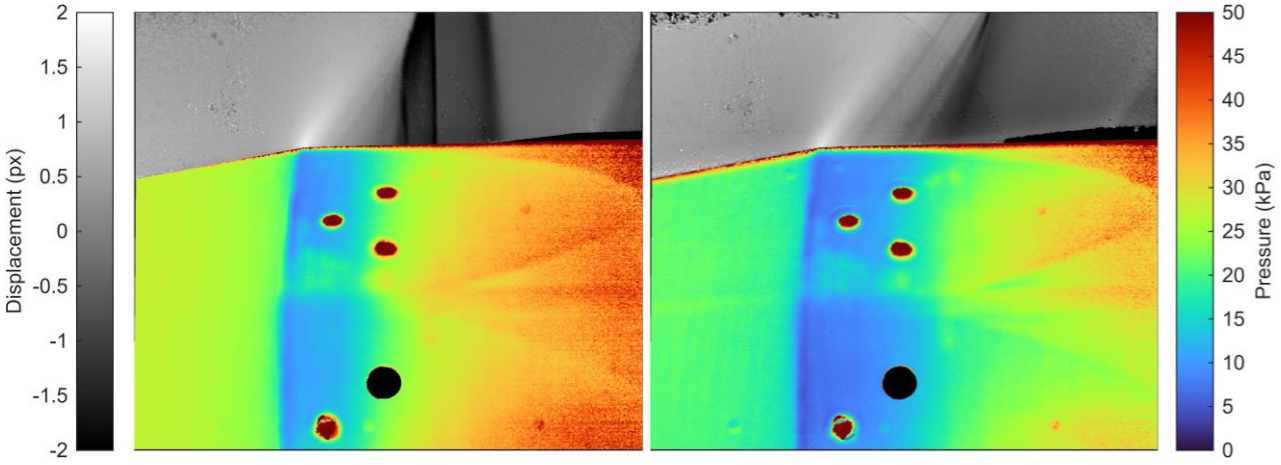


Figure 7 – Concurrent averaged BOS (grey) and PSP (colour) results from the downstream high-resolution camera (CX-25 B) at Mach 0.95 (left) and Mach 1.15 (right) at a roll angle of 0°.

The absolute pressure values, and the distributions, are highly sensitive to the quality of the calibration and other variables such as temperature. Pressure taps and CFD offer higher fidelity validation but starting with analytical predictions is a useful method to understand trends and the underlying physics. The static pressure can be determined via isentropic flows equations and compressible normal and oblique shock formulas. Upstream of the model the static pressure is related to the total pressure by an isentropic expansion process,

$$\frac{p_t}{p_0} = \left(1 + \frac{\gamma - 1}{2} M^2\right)^{\frac{\gamma}{\gamma - 1}} . \tag{2}$$

For a total pressure, p_t, of 60 kPa and γ of 1.4, by substitution, p_0 is 33.6 kPa for Mach 0.95 and p_0 is 26.4 kPa for Mach 1.15. Given the forebody facet half-angle is approximately 12° and the nose is blunted, the shock is expected to be a detached normal shock (no theta-beta-Mach solution) for supersonic Mach numbers, so the static pressure ratio across the shock is,

$$\frac{p_1}{p_0} = \frac{\left(2\gamma M^2 - (\gamma - 1)\right)}{(\gamma + 1)} . \tag{3}$$

Substitution gives p_1 of 36.3 kPa for Mach 1.15. In both Mach 0.95 and 1.15 conditions the PSP pressure is less than the analytical solution predicts. The normal shock pressure rise is not observed at all for the Mach 1.15 case with the PSP more closely matching the static pressure upstream of the shock.

The low PSP absolute pressure values may be explained by limitations and errors in the calibration, low signal-to-noise ratio, and temperature variation. Limits in the facility operating conditions prevented calibration below 40 kPa and since 60 kPa total pressure was selected to achieve sufficient signal-to-noise ratio, much of the pressure field falls in the extrapolated region of the calibration. Changing the reference pressure from the total pressure to the lowest calibrated pressure of 40 kPa slightly improves the lowest signal results but the results are not separable for higher signal areas. While increasing the test pressure would reduce extrapolation, the signal-to-noise ratio is already extremely low once the aperture is closed for concurrent BOS and PSP. The higher-resolution cameras have a smaller sensor than the Phantom v2640 and higher pixel density resulting in much less light collection per pixel. The mean fluorescence intensity is only 1% of the camera dynamic range during wind-on testing resulting in generally low signal to noise ratio. In the worst case, low illumination on the downstream region, combined with already low fluorescence at high calibration pressures, results in intensity measurements that overestimate fluorescence. This results in a lower gradient calibration curve which would predict a lower pressure for a given measured intensity in the low-pressure extrapolated region of the calibration. Though these factors contribute, the low-pressure PSP reading is most likely caused by temperature which is outlined in the following section.

4.2 Temperature effects

Lower temperatures result in higher paint fluorescence and lower computed PSP pressures [25]. Although the tunnel total temperature is controlled to 35 °C, flow expansion to reach the test condition reduces temperature isentropically and non-isentropic shocks create increase temperature. Non-uniform temperature distributions on the model correlate with static pressure; low pressures result in low temperatures and higher fluorescence. This results in pressure differences being overpredicted. Higher Mach numbers will have higher intensity PSP results, thus lower predicted pressures, as the static pressures are lower.

Returning to the theoretical analysis of the tunnel static temperature, the static temperature just upstream of the model, is related to tunnel static pressure by isentropic relations,

$$T_0 = T_t \left(\frac{p_0}{p_t}\right)^{\frac{\gamma-1}{\gamma}} . \tag{4}$$

Substituting the analytical pressures, results in T_0 = 264.1 K or -9.0 °C for Mach 0.95 and T_0 = 243.7 K or -29.4 °C for Mach 1.15. Then, in the Mach 1.15 case, the static temperature is rapidly increased by the non-isentropic normal shock through an adiabatic process,

$$\frac{T_1}{T_0} = \left(2\gamma M^2 - (\gamma - 1)\right)\frac{(\gamma-1)M^2+2}{(\gamma+1)^2 M^2} . \tag{5}$$

Substitution predicts a temperature T_1 of 267.2 K or -6.0 °C after the shock. Values of –6.0 °C and –9.0 °C are much lower than the calibrated condition of 35 °C so the PSP fluorescence will be stronger than if the surface was at the calibration temperature [25]. Thus the calculated pressure would be lower than the actual pressure. This 40 °C difference generates large error based on the ISSI calibration information pertaining to the temperature sensitivity of the PSP. In the lowest pressure region following the expansion fan, the static temperature will also be the lowest due to the isentropic acceleration of the air. PSP intensity is expected to read higher; but because of the aforementioned temperature effects, an erroneous lower-pressure value is given. Recalling that the objective of this theoretical analysis was to understand the very low pressures measured by the PSP, it is likely that low static temperature is the primary cause for error, with a low signal intensity contributing at the furthest downstream portion of the model and calibration extrapolation contributing the remainder. The temperature effects can be addressed in future work via simultaneous thermography measurement of surface temperatures or by using a dual-luminophore PSP formulation. Given the temperature sensitivity, absolute pressures should be interpreted cautiously.

Concurrent measurement of PSP and BOS has been demonstrated on a single camera however its application is constrained for large freestream models and will be better applied to smaller models. The next sections focus on optimising the PSP system focussing on a larger field of view and unsteady data acquisition using the Phantom v2640. Validation against the pressure transducers installed on the CFE and comparison with CFD is deferred to the wider field of view results.

4.3 Unsteady Global PSP Measurements

The Phantom v2640 configured for wide field-of-view and high-speed acquisition collected PSP data across the Mach and orientation range. As previously explained, the low spatial resolution meant any density gradient induced displacements for the BOS pattern were too small to detect. Without the depth of field compromises required for concurrent BOS and PSP application, the camera aperture can be opened, and the fluorescence intensity is reliably greater than 10% of the camera dynamic range. This also meant the selecting the reference pressure as 40 or 60 kPa had no difference on the results. The results for the Mach sweep test are shown in Figure 8. At and below Mach 0.9 the separated region after the tier 1 transition shoulder is small and the static pressure is high. From Mach 0.95 to 1.0 the static pressure decreases across the entire body and the low-pressure region at the tier 1 transition shoulder grows. From Mach 1.05 to M1.15 the static pressure begins to rise as it is compressed by the shock structures. The low-pressure region remains the same size, but the downstream recompression becomes sharper as the shock strengthens and becomes more oblique. BOS results from §4.1 visualise this stronger recompression shock at Mach 1.15. Data was also

successfully acquired for the various pitch and roll angles showing the expected trends but is not shown. The windward side of the model showed higher pressure than the leeward side and low-pressure regions on the leeward side of the edges caused by small edge vortices were visible. No separation or unsteady phenomena were observed.
The decreasing static pressure up to sonic conditions and then a rise in pressure for low supersonic conditions is expected from the analytical compressibility equations if a normal shock is assumed. Theta-Beta-Mach relation has no solutions for the steep cone angle below Mach 1.6 forcing a detached normal shock structure. Under supersonic conditions the normal shock compression increases the static pressure and temperature on the vehicle. On-board pressure tap measurements are best suited for validation of the absolute pressure values while CFD aids validation of the spatial distribution. Preliminary validation is provided in the next section.

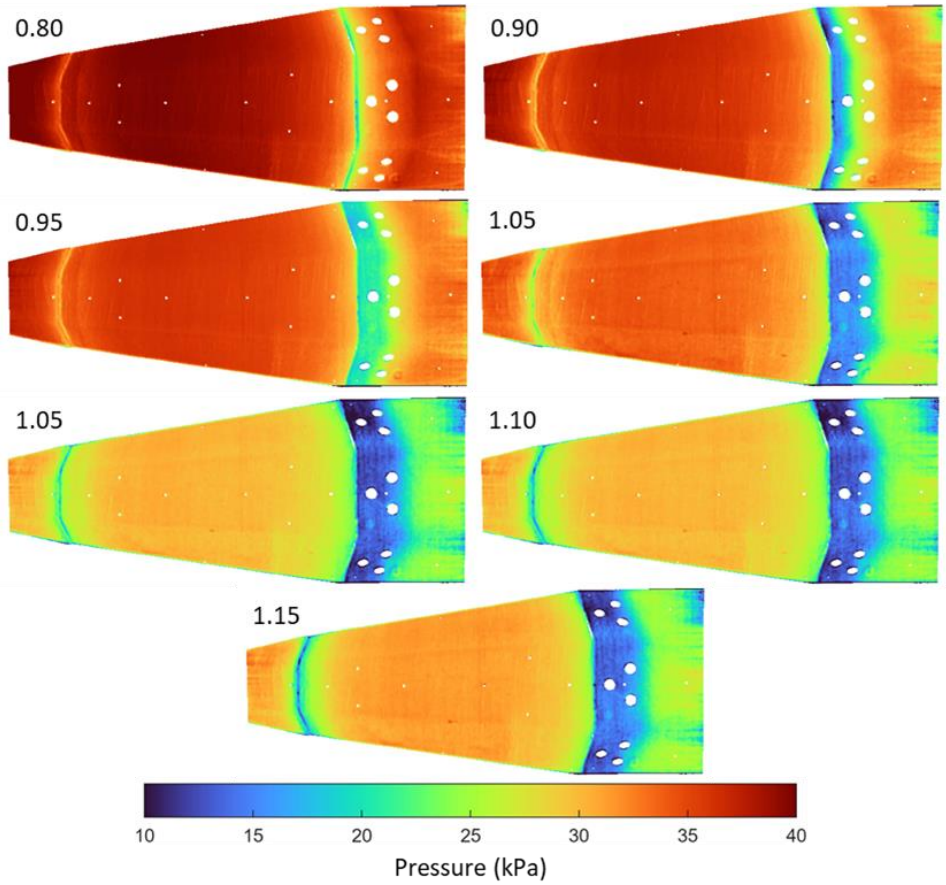


Figure 8 – Mean pressure fields for Mach 0.80 to 1.15 (Mach condition annotated on figure).

4.4 Validation against CFD and Pressure Taps

CFD was performed using Ansys Fluent with a Reynolds Averaged Navier Stokes (RANS) solver. The CFD analysis at Mach 1.15 and a total pressure of 60 kPa is presented in Figure 9. The overall pressure fields are qualitatively similar to the PSP results in §4.1 and §4.3. The CFD predicted the drop in pressure at the transition from the forebody to tier 1 would be larger than what the PSP results show suggesting the expansion fan is weaker than predicted. This could be due to the model roughness or the small lip on the experimental model not represented in the CFD. The low-pressure region behind the tier 1 transition shoulder is clear in the CFD, though the recompression is sharper and further downstream than in the PSP results. The complex interaction between the expansion fan and the recompression shocks may not have been captured in the simple RANS CFD. The CFD is consistent with the PSP results though the low-pressure region at the transition is again sharper and more uniform in the CFD than the PSP.

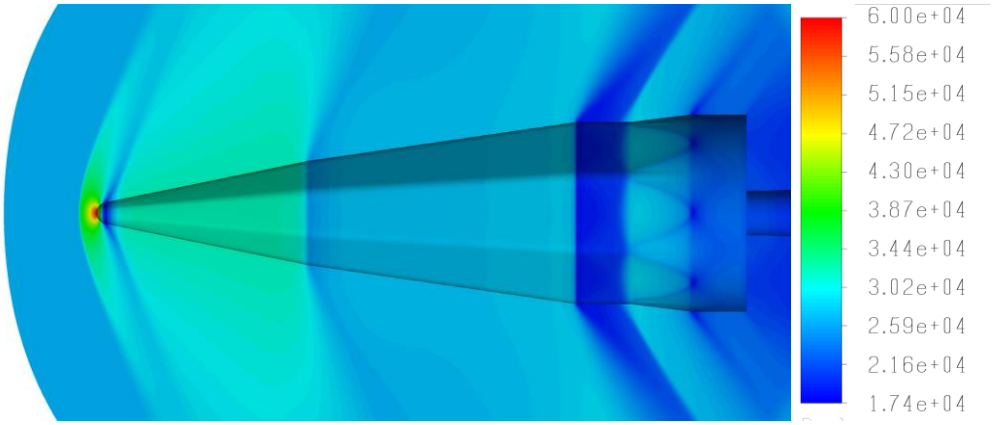


Figure 9 – Steady CFD RANS results of the pressure fields around the CFE at Mach 1.15 and 60 kPa total pressure at 0° pitch.

The preliminary pressure and temperature results collected concurrently with the BOS and PSP results during the Mach sweep are presented in Figure 10. The pressure tap measurements were expected to be a reference that could be used to validate and potentially correct the PSP results, and the thermocouples were expected to provide an indication of the temperature experienced by the paint. Seven of the eight forebody pressure taps were consistent with each other but lie outside the primary interest region for the PSP.

The two sets of 4 taps (taps 9-12 and 13-16) spaced along opposite sides of the tier 1 section produced results that were inconsistent between the sides and more varied than expected over a constant slope. The point measurements are higher than both the PSP and the CFD in all cases indicating the potential for leaks in the pressure tubing or porous structure within the model. The thermocouples measured temperatures closer to the total temperature rather than the model surface temperature suggesting their placement is too far from the surface for sufficient heat transfer. Investigation into the cause of these discrepancies are ongoing.

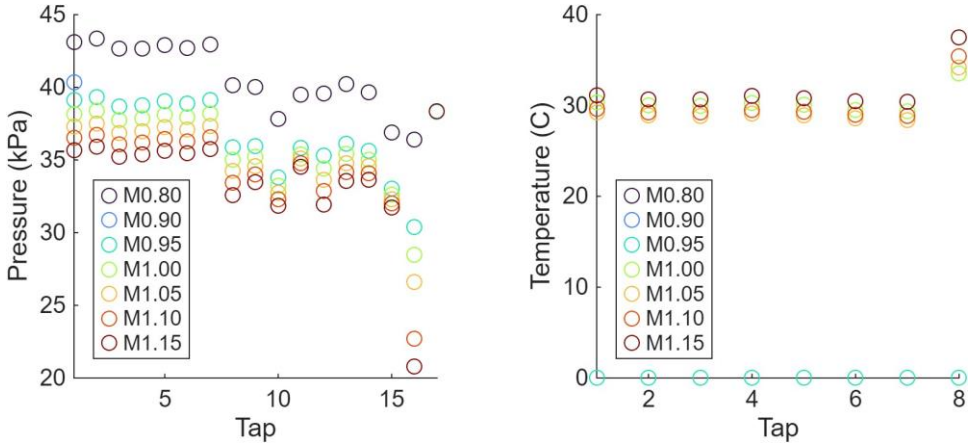


Figure 10 – Pressure (left) and temperature (right) point measurements for the Mach sweep.

4.5 Unsteady Measurements

High-resolution concurrent results in §4.1 found the flow exhibited some signs of unsteadiness in the BOS. Low signal to noise ratio for the PSP meant the unsteadiness was difficult to observe in the pressure field. High-speed measurements in §4.3 showed minimal natural unsteadiness in the PSP. This is expected because the pressure gradient is strongly favourable due to the steep cone angle on the CFE. To test the unsteady performance of the PSP capability, additional unsteadiness was introduced using a jet of air emanating from pressure tap 9.

Control jet actuators have been proposed as an engineering solution to high-speed control where conventional fin control creates high drag. Non-linear and unsteady behaviour is common for control jet actuators occurring in both the crossflow region and the downstream footprint. Reconfiguring one of the pressure taps (tap 9) to inject air provided an opportunity to study low mass flow control jets and test the unsteady performance of the PSP system. The jet pressure was set to 200 kPa with a total tunnel pressure of 60 kPa for a total pressure ratio of 3.3 and was driven by a cylinder of compressed instrument air. The tap 9 pressure transducer remained connected to the line confirming that the supply pressure was maintained through the facility tubing.
A local flow structure such as a small jet is difficult to image with both PSP and BOS from the same camera concurrently because the PSP requires a view orthogonal to the surface while BOS requires a view parallel to the surface. The change in the density gradient is very small and provides no insights beyond the injection region. The combined PSP and BOS results for the high-resolution camera presented in Figure 11 show the minimal influence of the jet. The results are the combined images from a model roll angle of 0° for the PSP, so the face is toward the camera, and 90° for the BOS, so the jet is orthogonal to the camera. The detected BOS disturbance is small and local, potentially only the barrel shock, with similar appearance between the two Mach numbers. In the PSP the pressure is seen to increase slightly upstream of the jet orifice and significantly decrease just downstream. Lower pressure is also evident as a downstream jet footprint beginning narrow and expanding as it develops. Though there is limited scientific insight from this data, it is apparent that the concurrent BOS/PSP system is sufficiently sensitive to detect these small changes.

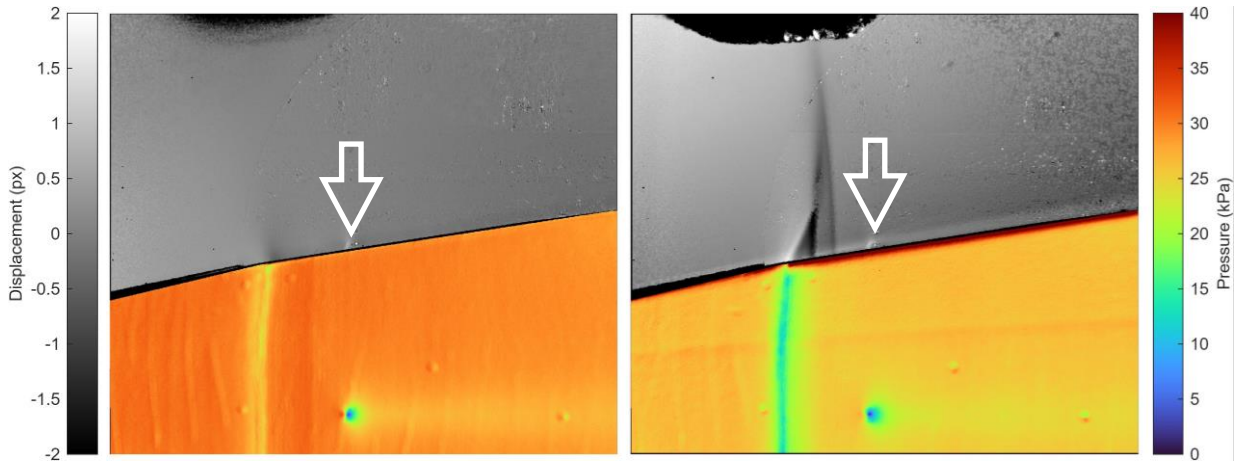


Figure 11 – High-resolution camera BOS and PSP at Mach 1.15 with the jet of air. The image is a composite image with the PSP (colour) taken with jet oriented toward the camera and the BOS (grey) taken when the jet is orthogonal after the model is rolled 90°. Arrow shows location of jet.

The high-speed camera captured the unsteadiness of the jet footprint as shown in Figure 12 in two image time-series of 11 successive frames captured at 3.0 kHz. The mean pressure field is shown with dashed outline indicating the extracted time series to visualise the unsteady jet flow dynamics. The top time series show the mean subtracted local pressure field with a pulsing jet flow motion while the bottom shows a lateral jet flapping motion. Although the 3.0 kHz acquisition rate was insufficient for robust temporal averaging, and already limited resolution is further reduced by a Gaussian filter to remove noise, the jet structures are visible. The Phantom v2640 remained configured for measurements of the full CFE so the results highlight the local performance is achievable without sacrificing field of view. The results clearly show the capability of the high-speed measurement system to capture complex, unsteady, small-scale pressure field data for detailed root-cause analysis whilst providing operationally relevant global performance results.

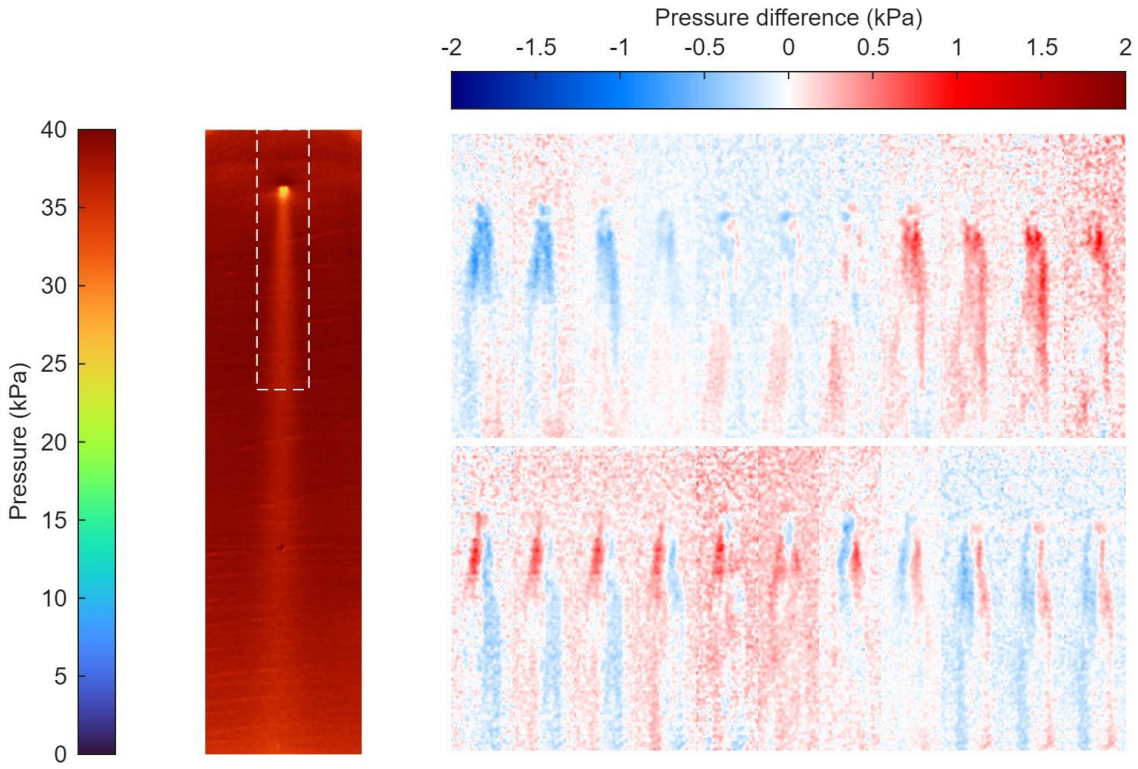


Figure 12 – Unsteadiness generated by the low-mass flow jet at Mach 0.95 and total pressure of 60 kPa is captured with PSP by the Phantom v2640 at 3.0 kHz. The mean pressure field (left) is shown with dashed outline indicating the extracted time series (right) to visualise the unsteady jet flow dynamics.

5. Discussion

High-resolution concurrent measurement of pressure and density fields showed consistency between the shock structures and their footprint. The capability is limited for global assessment of large freestream models because the required wide field-of-view makes the effective pixel size too large and reduces illumination flux on the surface. The offset between the PSP and BOS focal planes is also a major limitation since it requires closing the aperture to increase the depth of field and as a result markedly reduces the light available to the sensor. As such, this capability will be optimal for experiments using smaller models, models mounted on the sidewall, and for interrogating local regions of interest like control surfaces.

High-speed, wide field of view pressure fields were acquired using the Phantom v2640 with sufficient detail to investigate Mach and orientation dependence. Sufficient light was provided by the four pulsed 28 W Veritas Constellation 120EUV 385 nm lights to attain acceptable PSP emission signal levels for the current frame rates. Mach dependence matched analytical expectations with complicated interactions between the expansion fan and recompression shock at the junction between tier 1 and the transition sections. Insights into the transonic performance of the CFE hypersonic geometry were obtained and will support the development of CFE and other flight test vehicles.

Comparison between the PSP results, analytical calculations and CFD indicated that PSP discrepancies were primarily due to temperature gradients on the model. Low temperatures cause high fluorescence and a lower predicted pressure than if the static temperature was the same as the calibration temperature. All calibrations were taken at 35 °C static temperature whereas the actual static temperatures (for a total temperature of 35 °C) are –9 °C for Mach 0.95 and –6 °C for Mach 1.15 after a normal shock; and is the main reason for the apparent pressure increase for supersonic conditions. The expansion fan at the tier 1-transition interface is likely most influenced as it

accelerated the air, lowering the static temperature resulting in higher intensity. Despite a temperature difference of 40 °C between calibration and wind on, the PSP pressures are within 5 kPa of the CFD results. More work is required to remedy the observed temperature effects of the PSP for future unsteady measurements. Additional discrepancies in high-resolution PSP were likely caused by mean PSP intensity less than 1% of the camera dynamic range during wind on. Such a small intensity means signal-to-noise ratio is very low and may have falsely lowered the gradient of the calibration curve. Further consideration of these challenges, along with the extrapolation of the calibration curve to low static pressures, will be required for future testing.

Initial inspection of the forebody pressure tap measurements was inconclusive and inconsistent with both the PSP and CFD results. This is thought to be caused by porosity in the thin, additively manufactured pressure tapping features leaking pressure, but investigations are ongoing. Thermocouple measurements were also inconsistent with analytical surface temperature predictions probably due to the heat transfer properties of the model wall such that the cavity temperature of the model dominated the temperature at the sensor. The wind tunnel experiment has helped to test the onboard data acquisition system, but further development and validation is required.

No unsteadiness was observed in the CFE pressure field although some expansion fan and recompression shock unsteadiness was observed at the tier 1-transition junction in the BOS results. Investigation of a low mass flow jet on the model showed unsteadiness in the downstream pressure footprint. The very minor density gradient disturbance created by the jet was detected with the high-resolution imaging system. The high-speed imaging system acquired data at a sufficient rate and resolution to detect jet footprint structures and observe their development including the observation of pulsing and flapping jet motions. While the CFE pressure field was very steady, the control jet experiment demonstrated that the optical measurement system can acquire high-speed data with high spatial, temporal, and pressure resolution.

Aside from scientific value, the concurrent BOS and PSP on high-speed and high-resolution cameras provided logistical and operational benefits. Collecting both concurrently made file storage and camera settings easier and halved acquisition times. No changes to the optical or lighting setup during the primary test campaign window prevented misalignments and increased tunnel utilisation during the test window. Altogether, this configuration should satisfy the majority of the industrial test campaign requirements within the DSTG TWT. The simplicity and flexibility also reduced system cost and enable greater operator familiarity.

6. Concluding Remarks

This campaign demonstrated a novel, integrated experimental capability in the DSTG TWT, combining concurrent single-camera BOS and unsteady PSP measurements with onboard instrumentation and six degree-of-freedom force balance data. The alternating-frame acquisition approach represents a key innovation, enabling inherently aligned density-gradient and surface-pressure fields while overcoming the optical access and alignment limitations typical of industrial facilities. In addition, the dual-scale BOS implementation and coordinated high-speed/high-resolution imaging provide a flexible framework adaptable to a range of model scales and test objectives.

The use of a flight-representative hypersonic geometry provided a uniquely comprehensive dataset spanning local flow physics and global aerodynamic response. Despite limitations related to PSP temperature sensitivity, calibration range, and signal-to-noise constraints, the measurements showed consistent trends with theory and CFD and successfully captured key transonic flow features.

This work establishes a scalable framework for multi-modal aerodynamic testing. Future integration of unsteady pressure fields with force and moment measurements offers a clear pathway to link flow phenomena with aerodynamic loading, enabling deeper insight into transonic performance and flight-relevant behaviour of hypersonic vehicles.

7. Contact Author Email Address

Please direct all inquiries to the DSTG Experimental Aerodynamics team. Corresponding author: connor.marshall1@defence.gov.au.

8. Acknowledgements

This investigation was enabled by the provision of the CFE by UNSW Canberra and Lockheed Martin Australia. The CFE was developed with funding and support from Lockheed Martin Australia and the Defence Trailblazer, a collaborative partnership between the University of Adelaide and UNSW, supported by the Australian Government's Department of Education. The maintenance and operation of the Transonic Wind Tunnel is made possible by a dedicated team at DSTG led by the Facility Manager, Paul Tweedly, and the Wind Tunnel Operations Discipline Leader, Adam Blandford.

9. Copyright Statement

The authors and their respective organisations, hold copyright on all of the original material included in this paper. The authors permit the publication and distribution of this paper as part of the ICAS proceedings or as individual off-prints from the proceedings.

References

[1] Humphrey N, Huang H, Giacobello M and Manovski P. Development of a Background-Oriented Schlieren System for a Transonic Wind Tunnel. *23rd Australasian Fluid Mechanics Conference*, Sydney VIC, Australia, 2022. 395

[2] Lam S and Davies A. A Study of the Effects of Pressure Sensitive Paint on the Aerodynamic Drag of an AGARD Calibration Model B. *103rd Supersonic Tunnel Association International Meeting,* Buffalo NY, USA, 2005.

[3] Heath N, Neely A and Buttsworth D. Hypersonic Jet Interaction on an Axisymmetric Finned Vehicle Using Pressure Sensitive Paint. *AIAA Aviation Forum and ASCEND*, Las Vegas NV, USA, AIAA 2025-3722, 2025. DOI: 10.2514/6.2025-3722

[4] Gianellis N, Luppino J, Cousens S, Eldridge M, Smith J, van Pelt H, Wild G, Neely A, Beinke S, and Gorin S. The Common Front End: A Testbed Concept for High-Speed Technology Maturation. *AIAA SciTech 2025 Forum*, Orlando FL, USA, AIAA 2025-0550, 2025. DOI: 10.2514/6.2025-0550

[5] Avelar A, Basso E, Filho J, Romero P and Hsu J. Experimental and Numerical Analysis of the Flow Patterns around a Sounding Rocket in the Transonic Regime. *32nd AIAA Applied Aerodynamics Conference*, Atlanta GA, USA, AIAA 2014-3136, 2014. DOI: 10.2514/6.2014-3136

[6] Avelar A, Filho J and Silva L. Transonic Aerodynamics Analysis of Different Forebody Shapes of Aerospace Vehicles. *Journal of Aerospace Technology and Management*, Vol. 12, e1520, 2020. DOI: 10.5028/jatm.v12.1103

[7] Elizondo V, Dhanagopal A and Combs C. Fast-Responding Pressure-Sensitive Paint Measurements of the IC3X at Mach 7.2. *Aerospace*, Vol. 10, No. 10, 890, 2023. DOI: 10.3390/aerospace10100890

[8] Sellers M, Nelson M, Burnside N and Roozeboom N. Evaluation of Unsteady Pressure Sensitive Paint Use for Space Launch Vehicle Buffet Determination. *55th AIAA Aerospace Sciences Meeting*, Grapevine TX, USA, AIAA2017-1402, 2017. DOI: 10.2514/6.2017-1402

[9] Heaney P, Soranna F, Sekula M, Piatak D and Ramey J. Analysis of Transonic Unsteady Aerodynamic Environments using Unsteady Pressure Sensitive Paint for the Space Launch System Block 1 Cargo Launch Vehicle. AIAA SCITECH, Online, AIAA 2021-1833, 2021. DOI: 10.2514/6.2021-1833

[10] Chan D, Shea P, Goodliff S, Walker M, Collins J, Langston S, Mears L, Rieken E and Pinier J. Overview of the High Reynolds Number Ascent Wind Tunnel Test of the Space Launch System at the National Transonic Facility. *AIAA SCITECH,* National Harbor MD, USA, AIAA 2023-0425, 2023. DOI: 10.2514/6.2023-0425

[11] Rogers S, Dalle D and Chan W. CFD Simulations of the Space Launch System Ascent Aerodynamics and Booster Separation. *AIAA SCITECH,* Kissimmee FL, USA, AIAA 2015-0778, 2015. DOI: 10.2514/6.2015-0778

[12] Soranna F, Streett C, Heaney P, Sekula M, Piatak D, Goushcha O and Reamy J. A Database of CFD-Based Buffet Forcing Functions for Artemis I Structural Response Evaluation. *AIAA SCITECH*, Orlando FL, USA, AIAA 2025-1463, 2025. DOI: 10.2514/6.2025-1463

[13] O'Brien T and Lewis M. Rapid Transonic Aerodynamic Prediction for Hypersonic Lifting Bodies. *Journal of Aircraft,* Vol. 39, No. 6, pp. 1003-1013, 2002. DOI: 10.2514/2.3028

[14]Ueno A and Suzuki K. Two-Dimensional Shape Optimization of Hypersonic Vehicles Considering Transonic Aerodynamic Performance. *Transactions of the Japan Society for Aeronautical and Space Sciences,* Vol. 52, Iss. 176, pp. 65-73, 2009. DOI: 10.2322/tjsass.52.65

[15]Feng C, Chen S, Yuan W, Li Z and Gao Z. A wide-speed-range aerodynamic configuration by adopting wave-riding-strake wing. *Acta Astronautica,* Vol. 202, pp. 442-452, 2023. DOI: 10.1016/j.actaastro.2022.11.010

[16]Qu F, Wang T, Liu C, Fu J and Bai J. Aerodynamic shape optimization of the vortex-shock integrated waverider over a wide speed range. *Aerospace Science and Technology,* Vol. 143, 108696, 2023. DOI: 10.1016/j.ast.2023.108696

[17]Qu F, Wang X, Zhong J and Qu H. Aerodynamic design optimization of the hypersonic inward turning inlet in wide-speed range. *Physics of Fluids,* Vol. 36, Iss. 12, 7109, 2024. DOI: 10.1063/5.0234961

[18]Qiao N, Ma T, Jing B, Fu J and Zhang L. Design and aerodynamic analysis of the morphing waverider with rotating telescopic wing for wide-speed-range flight. *Aerospace Science and Technology,* Vol. 158, 109941, 2025. DOI: 10.1016/j.ast.2025.109941

[19]Smith J, Handford D, van Pelt H, Neely A and Brown S. The Aerothermal, and Structural Design of the Common Front End Flight Vehicle. *AIAA SCITECH,* Orlando, FL, USA, AIAA 2026-0105, 2026. DOI: 10.2514/6.2026-0105

[20]van Pelt H, Eldrige M, Handford D and Neely A. The Common Front End: Integrated Avionics, Diagnostics, and Standardised Measurement Interface for Hypersonic Flight Experiments. *AIAA SCITECH,* Orlando, FL, USA, AIAA 2026-0106, 2026. DOI: 10.2514/6.2026-0106

[21]Manovski P, Marshall C, Heath N and Neely A. Assessment of Dual-Scale Background Oriented Schlieren for Transonic Vehicle Aerodynamics. *25th Australasian Fluid Mechanics Conference*, Christchurch, New Zealand, 6-10 December 2026. Accepted.

[22]Crafton J, Forlines A, Palluconi S, Hsu K, Carter C and Gruber M. Investigation of transverse jet injections in a supersonic crossflow using fast-responding pressure-sensitive paint. *Experiments in Fluids,* Vol. 56, No. 27, 2015. DOI: 10.1007/s00348-014-1877-3

[23]Gehlen M. The centenary of the Stern-Volmer equation of fluorescence quenching: From the single line plot to the SV quenching map. *Journal of Photochemistry and Photobiology,* Vol. 42, 100338, 2020. DOI: 10.1016/j.jphotochemrev.2019.100338

[24]Huang C, Lin Y, Huan Y and Chung K. Pressure-sensitive paint measurements with temperature correction on the wing of AGARD-B under transonic flow conditions. *Measurement Science and Technology*, Vol. 32, No. 9, 094001, 2021. DOI: 10.1088/1361-6501/ac0073

[25]Woodmansee M and Dutton J. Treating temperature-sensitivity effects of pressure-sensitive paint measurements. *Experiments in Fluids*, Vol. 24, pp. 163-174, 1998. DOI: 10.1007/s003480050163

[26]Peng D, Jensen C, Juliano T, Gregory J, Crafton J and Palluconi S. Temperature-Compensated Fast Pressure-Sensitive Paint. *50th AIAA Aerospace Sciences Meeting,* Nashville, TN, USA, AIAA2012-1186, 2012. DOI: 10.2514/6.2012-1186